A New Dioxasilepine–Aryldiamine Hybrid Electron-Blocking Material for Wide Linear Dynamic Range and Fast Response Organic Photodetector

by Kai-hua Kuo

A New Dioxasilepine−Aryldiamine Hybrid Electron-Blocking Material for Wide Linear Dynamic Range and Fast Response Organic Photodetector

Kai-Hua Kuo,[||] Richie Estrada,[||] Chih-Chien Lee, Nurul Ridho Al Amin, Ya-Ze Li, Marvin Yonathan Hadiyanto, Shun-Wei Liu,* and Ken-Tsung Wong*

Cite This: ACS Appl. Mater. Interfaces 2022, 14, 18782−18793

Read Online

ACCESS | Metrics & More | Article Recommendations | SI Supporting Information

ABSTRACT: A new dioxasilepine and aryldiamine hybrid material **DPSi-DBDTA** is designed to act as the electron-blocking layer (EBL) for vacuum-processed organic photodetector (OPD). The O−Si−O-linked cyclic structure leads **DPSi-DBDTA** to have dipolar character, high LUMO, and good thermal and morphology stability suitable for vacuum deposition. An initial trial with C_{60}-based single active layer OPD device manifests the superior capability of **DPSi-DBDTA** for dark current suppression compared to the typical aryldiamines. Here, the bare and MoO_3-doped **DPSi-DBDTA** is further examined as EBLs for the visible light responsive OPD comprising **DTDCPB**/C_{70} bulk heterojunction (BHJ) as the active layer. In sync with the result of C_{60}-based OPD, the low dark current density and high specific detectivity D^* (7.085×10^{12} cm $Hz^{1/2}$ W^{-1}) are achieved. The device with 5% MoO_3-doped EBL can exhibit a wide linear dynamic range (LDR) up to 154.166 dB, which is attributed to suppression of both dark current density and carrier recombination. Additionally, the devices also manifest fast time-resolved performance in both frequency and transient response measurements. Especially for the device with 20% MoO_3-doped EBL, a wide cutoff frequency response 692.047 kHz and record-high transient response demonstrating ≤0.683 μs for transient photovoltage (TPV) and ≤0.478 μs for transient photocurrent (TPC) have been realized, which is possibly owing to the balance of mobility that mitigates the damage from traps. Such submicrosecond response is comparable with the state-of-the-art perovskite-PDs and Si-PDs.

KEYWORDS: vacuum-deposited photodetector, electron blocking material, dioxasilepine, DTDCPB:C_{70} active layer, wide linear dynamic range, fast response OPD
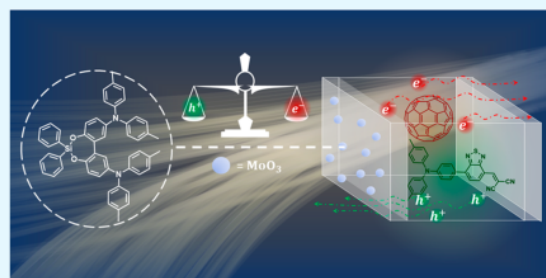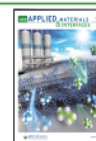
1. INTRODUCTION

Organic photodetectors (OPDs) that convert the light signal into electric current under a bias have gained significant research interest due to their various applications such as large-area sensing, biomedical imaging, and flexible mobile displays.[1−3] Particularly, OPD integrating with other organic electronics can create innovative sensing systems. For example, a flexible display incorporating OPD and organic light-emitting diode (OLED) demonstrated the capability of capturing a fingerprint image. The flexibility of organic materials ensures the device works persistently under deformation and renders high image accuracy and good resolution feasible.[4] In addition, a 1 cm² ring-shaped OPD-based photoplethysmogram (PPG) sensor with comparable performance of Si-based photo-detector (Si-PD) has been realized very recently for large-area flexible biometric monitoring application.[5] Although these examples reveal the advantages and prospects of OPDs, some intrinsic challenges, including stability issues, undamped noise sources, high dark current, narrow linear dynamic range

(LDR), and slow response time, still remain to be solved. The active layer of OPD can be fabricated by either solution or vacuum process similar to other organic devices like OLEDs and organic photovoltaics (OPVs). The successful commercialization of OLED technology reveals the advantage of the vacuum process for conquering the stability issue of organic electronics. Recent studies on vacuum-processed OPVs indicate that the suppression of charge carrier recombination that eventually leads to superior photoconversion efficiency can be achieved with tailor-made photoresponsive small molecules.[6] It is thus believed to be beneficial for the OPDs active layer design. To unlock the limitation of dark current,

the interlayers (known as blocking layers)[7−9] introduced between the active layer and the electrode have been employed to block injection of electrons from the anode to LUMO of the acceptor and holes from the cathode to the HOMO of the donor under a reverse bias voltage. A wide LDR would be realized by simultaneously achieving low total noise currents (shot and thermal) in conjunction with high photoconversion efficiency. Finally, the response time of OPDs can be effectively enhanced along with the improvement of carrier transportation and extraction efficiency, which is closely related to carriers' mobility and recombination issues within the whole device. Therefore, to achieve a superior OPD exhibiting comparable or even better characteristics than Si-PDs, appropriate molecular designs of not only the active layer but also the blocking layer are highly desired.

Typically, a material suitable for the electron-blocking layer (EBL) needs to have a high LUMO energy level to block the direct electron injection and nice mobility for fast and efficient hole transportation.[7] Typical hole-transporting materials[8,10−14] commonly used in OLEDs are suitable EBLs for OPD, leading to good dark current suppression to 10^{-9} A cm^{-2} level. The vacuum-processable EBL should have limited molecular conjugation to give high LUMO and suitable HOMO and sufficient thermal and morphological stability. In this study, a new electron-blocking material **DPSi-DBDTA** with dioxasilepine−triarylamine hybridized structure was developed to improve the vacuum-deposited OPD performance. The introduction of O−Si−O-linked cyclic structure twists the aryl core and brings in the dipolar character of the molecule. **DPSi-DBDTA** exhibits a high LUMO, suitable hole-transport, and good thermal and morphological stability. For a trial, the electron-blocking capability of **DPSi-DBDTA** was initially tested by employing C$_{60}$ as the single active layer. The superiority in suppressing dark current density was observed down to the order of 10^{-11} (A cm^{-2}), which outperforms the conventional triarylamine-based EBLs. After demonstrating its promising potential, **DPSi-DBDTA** was further employed as EBL of the OPD device configured with a bulk-heterojunction (BHJ) active layer for comprehensive visible spectral response and better photoconversion efficiency. The optimal device manifests high external quantum efficiency (EQE) as well as very low dark current density, which eventually results in a specific detectivity (D^*) up to 7.085×10^{12} cm Hz$^{1/2}$ W^{-1}. Further, by the aid of metal oxide (MoO$_3$) doped in **DPSi-DBDTA**, the device, to our surprise, shows an excellent LDR (154.166 dB) and very rapid response behavior (t_{Fall} = 0.683 μs). These features not only involve the acceleration of charge (hole) transporting inside EBL but also the carrier balancing issue, which is closely related to the molecular interaction between **DPSi-DBDTA** and MoO$_3$. Overall, the outstanding performance comparable to the state-of-the-art Si-PDs reveals the bright future of design strategies for vacuum-processed OPDs.

2. RESULTS AND DISCUSSION

The synthesis of target molecule **DPSi-DBDTA** is shown in Scheme 1. The synthetic procedures and characterizations are reported in the Supporting Information. The precursor **2** was synthesized via Pd-catalyzed Buchwald−Hartwig amination reaction from a reported compound **1**.[15] Then, the demethylation of **2** with boron tribromide gave the intermediate **3** with a good yield. Compound **3** underwent a base-catalyzed condensation reaction with Ph$_2$SiCl$_2$, leading to

Scheme 1. Synthetic Pathway of New Electron-Blocking Material DPSi-DBDTA
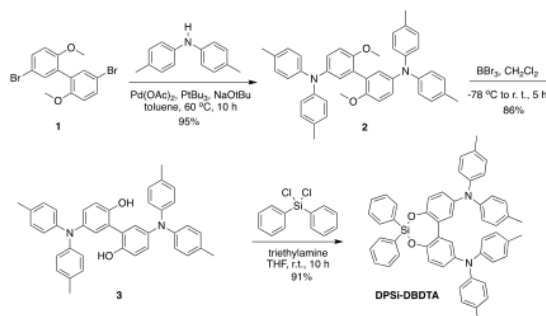
the desired **DPSi-DBDTA** containing a seven-membered siloxy ring (dioxasilepine). The desired target compound was purified by reprecipitation and then vacuum sublimation before characterization and device fabrication. The thermal stability of **DPSi-DBDTA** was studied with thermogravimetric analysis (TGA), where the decomposition temperature (T_d) relative to 5% weight loss was recorded as 373.54 °C (Figure S1). The high T_d reveals that **DPSi-DBDTA** is suitable for vacuum deposition. Differential scanning calorimetry (DSC) was conducted for probing morphological stability of **DPSi-DBDTA**. From the DSC trace (Figure S2), the glass transition temperature (T_g) was assigned to be 101.60 °C.

The electronic absorption spectrum (Figure 1a) of **DPSi-DBDTA** in toluene displays a λ_{max} centered at 305 nm, which was assigned to the $\pi-\pi^*$ transition, and a broad low-energy absorption centered at around 360 nm corresponding to the intramolecular charge transfer (ICT) transition. The emission spectrum of **DPSi-DBDTA** was recorded in toluene, giving photoluminescence (PL) centered at ~405 nm. From the crossing point of absorption and emission spectra, the optical energy gap (E_g) was calculated to be 3.28 eV. The wide E_g of the blocking material provides high transparency in the visible range, which could prevent the EQE reduction of the OPD device.[16,17] Herein, the electrochemical property of **DPSi-DBDTA** was studied with cyclic voltammetry (CV). The voltammogram (Figure 1b) displays consecutive quasi-reversible oxidations with the half-potential assigned at 0.52 and 0.64 V. By reference to the redox potential of ferrocene, the HOMO level was calculated to be −5.31 eV. In contrast, the LUMO energy level of −2.03 eV was then calculated with E_g added to the HOMO. **DPSi-DBDTA** shows a high LUMO level, which is one of the essential properties for serving as electron-blocking materials. Interestingly, the high LUMO energy level seems to be correlated with introduction of the dioxasilepine ring, which can be manifested by theoretical calculation.

The theoretical analysis of **DPSi-DBDTA** was conducted through density functional theory (DFT), which was carried out at the B3LYP/6-31G (d,p) level. The optimized structure and the HOMO/LUMO population distribution are depicted in Figure 1c. The population of HOMO is mainly delocalized over the *p*-ditolylamine moiety and the biphenyl core, while the dioxasilepine and the biphenyl core contribute to the LUMO population. The spatially separated HOMO and LUMO distributions rationalize the low energy electronic transition (S$_0$ to S$_1$) with CT character. In addition, the dipolar nature of the molecule leads to the separated electron-/hole-
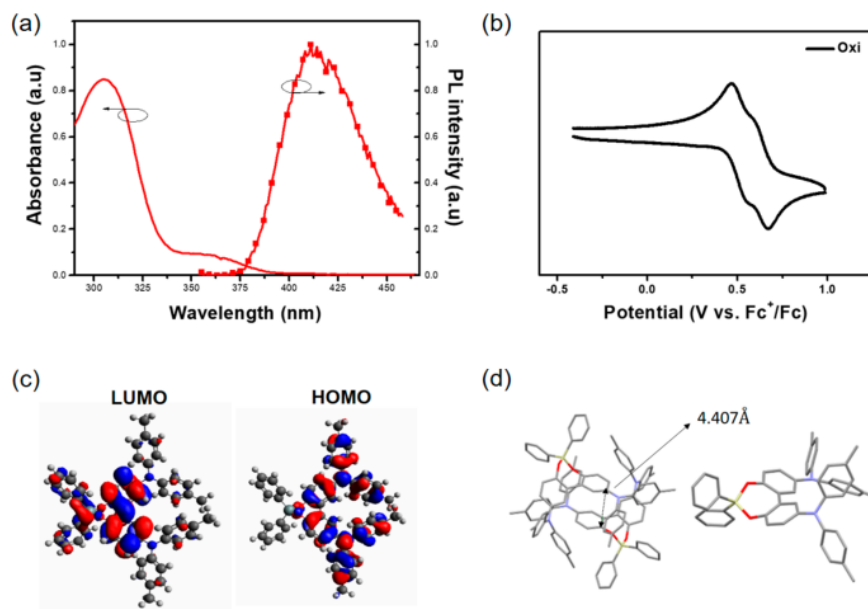
Figure 1. (a) UV−vis absorption and photoluminescence spectra in toluene solution, (b) cyclic voltammograms, (c) DFT calculated HOMO and LUMO populations, and (d) single crystal structure of **DPSi-DBDTA**.
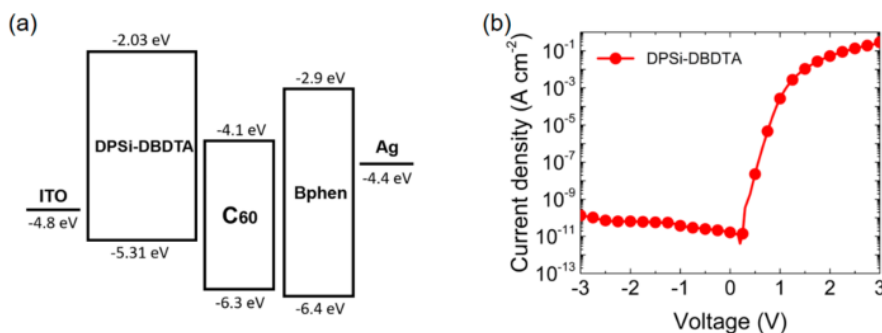

Figure 2. (a) Energy level diagram and (b) current density−voltage (J−V) characteristic (dark condition) based on the structure layer of ITO/**DPSi-DBDTA**/C_{60}/Bphen/Ag by sweeping the bias from 3 to −3 V.

transporting channel, with ditolylamine moiety dominating the hole transport and the dioxasilepine moiety governing the electron-transporting behavior. Observationally, the molecular structure and crystal packing of **DPSi-DBDTA** were characterized by single-crystal X-ray crystallography (Figure 1d). Here, suitable crystals were obtained by slow diffusion of orthogonal solvents (toluene/hexane) and evincing the twisted biphenyl core of **DPSi-DBDTA** with a dihedral angle of 38.05°, rendering the dioxasilepine ring to have a nonplanar structure. The donor−acceptor molecular structure leads **DPSi-DBDTA** to pack into an antiparallel manner. However, the nonplanar structure prevents severe intermolecular interactions. The closest distance between two neighboring π core (C8 and C'11) is about 4.4 Å, which is not close enough to exhibit π−π interaction. The antiparallel arrangement had been reported to effectively cancel molecular dipole moments in the solid state, thus avoiding the large energetic disorder,[6,18,19] potentially benefiting transportation behavior.

To test the electron blocking capability of **DPSi-DBDTA**, a standard OPD device was fabricated by considering the cascade of energy level between the active layer and electrode as represented in Figure 2a. The device was composed of an active layer (C_{60}) sandwiched between the carrier blocking layers and electrodes. Herein, the performance of an EBL relies on the ability to minimize the dark currents under a reverse bias. Figure 2b shows the current density−voltage characteristic for the OPD device with the EBL thickness of 20 nm measured under dark conditions by sweeping the bias from 3 to −3 V. Surprisingly, a great dark current suppression is observed with a value $\sim 10^{-11}$ A cm^{-2} under −1 to −2 V and maintained at 1.35×10^{-10} A cm^{-2} under −3 V reverse bias. As compared to commercial EBLs, N,N'-bis(1-naphthyl)-N,N'-diphenyl-1,1'-biphenyl-4,4'-diamine (**NPB**), and 4,4'-(cyclohexane-1,1-diyl)bis-[N,N-bis(4-methylphenyl)aniline] (**TAPC**), the dark current suppressed by **DPSi-DBDTA** is lower (see Figure S3), which reveals its potential application. Therefore, it triggered our attempt to examine its applicability
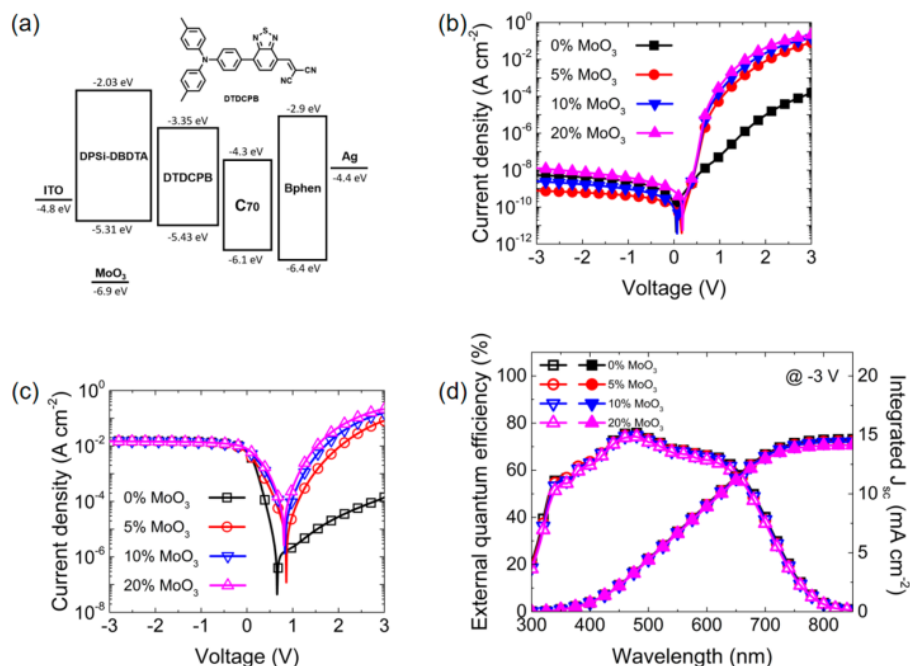
Figure 3. (a) Energy level diagram of the visible-responsive OPD, and the chemical structure of **DTDCPB**. Characteristics of current density–voltage (J–V) under (b) dark and (c) 1 sun illumination. (d) EQE spectra and integrated J_{SC} at a biased mode of −3 V for the OPD devices with various doping percentages of MoO_3.

in visible-light-responsive, BHJ-type OPD. Recently, the D–A–A′ configured donor material **DTDCPB** has been demonstrated to have remarkable efficiency in vacuum-deposited OPV when blended with C_{70} or C_{60} as the BHJ-type active layer.[6] The great performance for photoinduced charge carrier generation thus gives a promising potential for OPD application. Combined with our newly designed EBL, **DPSi-DBDTA**, the visible-light-responsive OPD device was designed, where the structure and corresponding energy level diagram are shown in Figures 3a and S4a.

In addition, this study introduced metal oxide as a conductivity dopant in EBL to improve transportation behaviors. To date, metal oxides have often been used to enhance hole extraction or injection in organic electronic devices.[20,21] Apart from modifying the barriers between the electrode and organic materials, most studies disclosed that the presence of metal oxides could also reduce leakage current when serving as an interlayer, yet the detailed mechanism is unclear.[20] Such an effect has been pointed out in Figure S5, where molybdenum trioxide (MoO_3) and tungsten trioxide (WO_3) were introduced into the traditional EBL, TAPC, maintaining or even enhancing leakage current suppression. This syncs with the previous studies reported by Lee et al., where 10% MoO_3-doped TAPC reduces the leakage electron injection with the increment of hole transport efficiency under the reverse bias.[13] Due to these capabilities, the metal oxide is thereby employed in this work.

The carrier transporting behavior in **DPSi-DBDTA**:MoO_3 bulk was investigated under different MoO_3 doping concentrations. The results show enhancement of charge carrier mobility (electrons and holes) along with the increment of MoO_3 doping percentage (Figure S6). As summarized in Table 1, on the basis of the space charge limited current (SCLC) measurement result, the electron mobility of bare EBL is 1.418

Table 1. Fitting Results of the Corresponding Electron and Hole Mobilities[a]

MoO_3 doping percentage [%]	electron mobility [cm^2 V^{-1} s^{-1}][b]	hole mobility [cm^2 V^{-1} s^{-1}][c]
0	1.418×10^{-12}	2.390×10^{-6}
5	1.213×10^{-6}	3.693×10^{-6}
10	2.750×10^{-6}	5.162×10^{-6}
20	4.924×10^{-6}	7.250×10^{-6}

[a]Measured under an electric field. [b]800–900 $V^{1/2}$ $cm^{-1/2}$. [c]600–700 $V^{1/2}$ $cm^{-1/2}$.

$\times 10^{-12}$ cm^2 V^{-1} s^{-1}, while the hole mobility of bare EBL is 2.390×10^{-6} cm^2 V^{-1} s^{-1}. As expected, the high HOMO level of **DPSi-DBDTA** results in much faster hole transportation. The introduction of MoO_3 dopant onto EBL improves the electron mobility up to the same magnitude as the hole mobility. This facilitates carrier transportation, but it may lead to concern of inferior electron blocking capability of the EBL.

The characteristics of current density–voltage for the visible-light-responsive OPDs with different doping percentages of MoO_3 are measured under the applied voltage biases of −3 to 3 V and presented in Figures 3b and S4b. In tune with the result observed in the single active layer OPD, the energy gap difference between the work function of ITO and the LUMO of **DPSi-DBDTA** creates a barrier that prevents the electron injection from the anode, thereby reducing the dark current density. However, the dark current density, surprisingly, tends to decrease from the device with bare EBL to the EBL doped with 5% MoO_3, then slightly increases with 10%
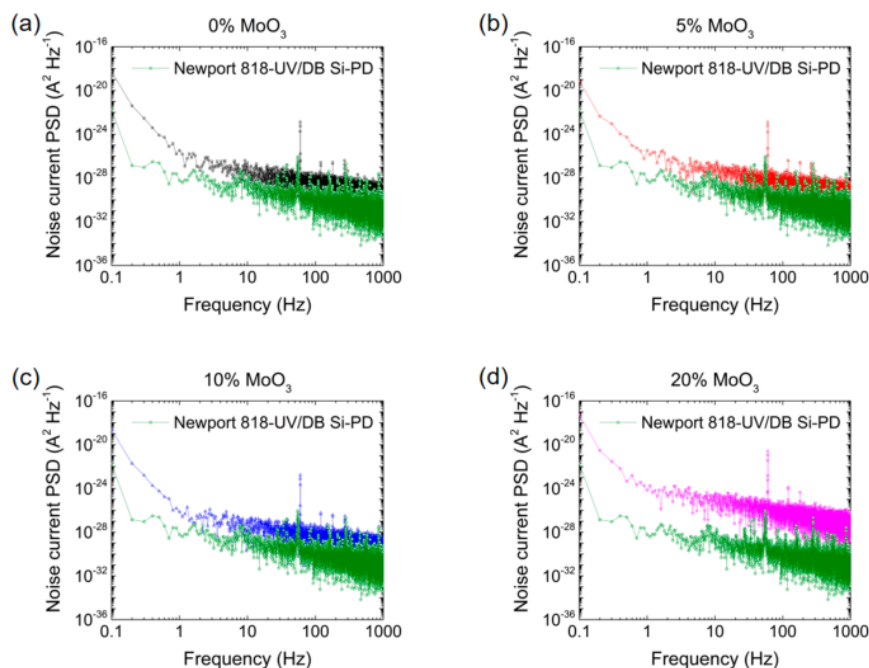
Figure 4. White noise current power spectral density versus frequency of the device doped with (a) 0%, (b) 5%, (c) 10%, and (d) 20% of MoO_3 at a biased mode of -3 V. The Si-PD of Newport 818-UV/DB is also measured as the green line for comparison.

and 20% dopant. It seems to contradict the mobility measurement result, where the EBL with faster electron mobility instead shows better electron blocking capability and lower dark current density. This is similar to the results mentioned in Figure S5, where low concentration metal oxide dopant in EBL may facilitate electron blocking capabilities. As have been well studied, the metal oxide such as MoO_3 or WO_3 would form deep defect/gap states and facilitate electron transportation through a tunneling mechanism, especially in the case with a single, neat interlayer of metal oxide, where the interface of organic material is heavily doped.[22−25] However, such a mechanism is not expected to be significant under low doping concentration when blending with organic materials. Moreover, the work function of EBL would be polarized and generate a so-called dipole interlayer with a tilted band structure.[24−26] This can be evidenced by the increase of open-circuit voltage (V_{OC}) when MoO_3 dopant is introduced, which will be discussed in detail in the next section. Competition between electron tunneling via gap state and polarization effect thus leads to the optimal doping concentration, in this case, 5% MoO_3, to achieve the lowest dark current density at 7.804×10^{-10} A cm^{-2}.

Under 1 sun illumination, the photogenerated carriers are extracted from the active layer toward electrodes (see Figures 3c and S4c). To evaluate the extraction, the integrated measurements are presented in the form of plots of the short-circuit photocurrent density from EQE ($J_{SC,EQE}$) under an applied bias of -3 V, as shown in Figures 3d and S4d. The devices with **DTDCPB**:C$_{70}$ active layer exhibit $J_{SC,EQE}$ values of 14.620, 14.458, 14.413, and 14.132 mA cm^{-2} with MoO_3 doped percentage at 0%, 5%, 10%, and 20%, respectively, while the devices comprised of **DTDCPB**:C$_{60}$ active layer also show a similar trend under a bias of -3 V, yet with overall inferior

$J_{SC,EQE}$ of 11.052, 10.882, 10.758, and 10.635 mA cm^{-2} for doping percentages of MoO_3 at 0%, 5%, 10%, and 20%. The slight degradation of photocurrent density, J_{ph}, along with the increment of doping concentration (see Figure S7 for details) points out the trade-off between carrier speed and recombination through gap states in EBL. This is owing to the lower EQE around 500 nm, which is the major absorption region for C$_{70}$.[27] Notably, the V_{OC} values of the devices (the discontinuous point in Figure 3c; see Figure S8 for detail) show significant enhancement, from around 0.662 to 0.859 V, in the presence of MoO_3. Due to V_{OC} being closely related to the built-in potential of the device, we thus attributed the enhancement of V_{OC} to the polarization of EBL.[25,28] Moreover, such a polarization effect originates from the participation of MoO_3 dopant. This not only consolidates our hypothesis that the MoO_3-doped **DPSi-DBDTA** acts like a dipole interlayer but also alleviates the concern about its electron blocking capability. To further study the molecular interaction between **DPSi-DBDTA** and MoO_3, atomic force microscopy (AFM) measurement was carried out. As presented in Figure S9, the surface roughness gradually increases along with increasing dopant concentration of MoO_3. It may imply that with more MoO_3, molecules (both **DPSi-DBDTA** and MoO_3) tend to aggregate with each other and result in stronger phase separation, better crystallinity, and thus faster carrier mobility.[29]

Noise is one of the most essential parameters that should be included in evaluating the performance of OPD. Figure 4 depicts the noise current power spectral density (PSD)− frequency measurements with different doping percentages under the bias of -3 V. Subsequently, the root-mean-square (RMS) of current noise could be determined by the following equation[30,31]

Table 2. Device Characteristics J_d, EQE, R, $i_{white,RMS}$, and D^* of OPD Devices Incorporating DPSi-DBDTA as EBL Doped with MoO$_3$

MoO$_3$ doping percentage [%]	J_d [A cm^{-2}][a]	EQE [%][b]	R [A W^{-1}][b]	$i_{white,RMS}$ [A][c]	D^* [cm Hz$^{1/2}$ W^{-1}][d]
0	$5.263 \times 10^{-9} \pm 2.654 \times 10^{-10}$	70.397 ± 0.098	$0.301 \pm 4.185 \times 10^{-4}$	2.549×10^{-13}	7.085×10^{12}
5	$7.804 \times 10^{-10} \pm 3.939 \times 10^{-11}$	70.146 ± 0.090	$0.300 \pm 3.839 \times 10^{-4}$	2.795×10^{-13}	6.440×10^{12}
10	$2.491 \times 10^{-9} \pm 1.420 \times 10^{-10}$	69.570 ± 0.110	$0.297 \pm 4.689 \times 10^{-4}$	3.084×10^{-13}	5.778×10^{12}
20	$1.289 \times 10^{-8} \pm 1.554 \times 10^{-10}$	69.040 ± 0.202	$0.295 \pm 8.628 \times 10^{-4}$	4.036×10^{-12}	4.386×10^{11}

[a]The data were obtained at a reverse bias voltage of −3 V. [b]The point spectra were acquired from the measurement under an excitation of 530 nm with a biased voltage mode of −3 V. [c]On the basis of the signal in Figure 4, the data are calculated by using eq 1, where f_1 = 100 Hz and f_2 = 1 kHz. [d]The data are obtained by using eq 4, where A = 0.04 cm^2 and Δf = 900 Hz (from 10^{-1} to 1 kHz).

$$i_{n,RMS} = \sqrt{\int_{f_1}^{f_2} i_n^{\,2}\, df} \qquad (1)$$

where f_1 and f_2 are respectively lower and upper bandwidth limits of frequency. i_n^2 is the current noise for either white or thermal power spectral density (A^2 Hz^{-1}). Here, the lower and upper frequency limits are set to be f_1 = 100 Hz and f_2 = 1 kHz. On the basis of eq 1, the white noise current increases gradually with the increment of the doping percentage of MoO$_3$, from 2.549×10^{-13} to 4.036×10^{-12} A (see Table 2). Regarding its opposite trend compared with dark current, it triggered us to explore the origin of noise sources further. Usually, the total noise can be divided into three parts: flicker (1/f), shot, and Johnson−Nyquist (thermal) noise. Flicker (1/f) is emergence at low frequencies yet negligible beyond the frequency of 100 Hz.[13] Shot noise describes the statistical fluctuation of current arising from dark current,[31−34] expressed by[9,30−32,35−38]

$$i_{shot} = \sqrt{2qI_d\Delta f} \qquad (2)$$

where q is an elementary charge (1.602×10^{-19} C), I_d is dark current (A), and Δf is the noise bandwidth (Hz). Accordingly, shot noise follows the same trend as dark current density, decreasing first (0−5%) and then increasing (5−20%) along with the increment of MoO$_3$ doping concentration. Thermal noise is obtained by noise current PSD−frequency measurements under unbiased voltage (0 V) conditions (Figure S10), which can be verified through the magnitude of shunt resistance, R_{Sh},[31−33,35] and calculated by[5,30,31]

$$R_{Sh} = \frac{4kT\Delta f}{(i_{thermal,RMS})^2} \qquad (3)$$

where k is the Boltzmann constant (1.381×10^{-23} J K^{-1}), T is the temperature (K), and $i_{thermal,RMS}$ is the RMS of current thermal noise (A). As shown in Table S1, the calculated R_{Sh} value is 0.402, 0.410, 0.358, and 0.307 GΩ for the introduced MoO$_3$ of 0%, 5%, 10%, and 20%, respectively. According to the equivalent circuit model developed by Prince (P-model), the value of R_{Sh} indicates the extent of photogenerated charge carriers' loss through an alternate pathway, which is majorly related to the leakage due to defects in the BHJ active layer.[5,6,13,39]

The largest R_{Sh} of the device with 5% MoO$_3$-doped EBL reveals a similar trend with dark current density, which indicates that besides the suppression of dark current from the anode, the introduction of MoO$_3$ also more efficiently prevents carrier leakage from the active layer. This is also a typical characteristic of the dipole-interlayer,[25] which further confirms our understanding of the functionality of MoO$_3$-doped **DPSi-DBDTA**. On the basis of our above analysis, both shot noise

(dark current) and thermal noise follow the same trend along with the doping concentration, violating the trend observed in white noise measurement. This points out another noise source existing here (frequency-dependent g-r noise, for example), yet it is brutal to identify or decouple using the conventional method. Several studies have denoted that the deviation from the conventional methods may happen under low noise situations,[36,40,41] which indicate that better accuracy should rely on the direct measurement results.

To identify the capability of OPD device within detection of the weakest photosignal, defined as the specific detectivity (D^*), Figure 11a,b provides the measured results of EQE and responsivity at the applied bias of −3 V. D^* would thereby be obtained via the following equation[30]

$$D^* = \frac{R\sqrt{A\Delta f}}{i_{white,RMS}} \qquad (4)$$

where R is the responsivity (A W^{-1}), A is the area of OPD device (cm^2), and $i_{white,RMS}$ is the RMS of white noise current (A). Among these devices (see Table 2 for details), the best D^* is 7.085×10^{12} cm Hz$^{1/2}$ W^{-1} at the wavelength of 530 nm under a bias of −3 V for the OPD device with the bare EBL. In contrast, the lowest D^* of 4.386×10^{11} cm Hz$^{1/2}$ W^{-1} was obtained for the device with the blocking layer doped with 20% MoO$_3$, which is caused by the high value of $i_{white,RMS}$. Intriguingly, the calculation is prone to be ascribed from combining the different noise contribution for D^* by the following equation[30,32]

$$D^* = \frac{R\sqrt{A\Delta f}}{\sqrt{\left(2qI_d + \frac{4kT}{R_{Sh}}\right)\Delta f}} \qquad (5)$$

As summarized in Table 2 and Table S1, the use of both eqs 4 and 5 gives pointedly different results, as can be seen in Figure S11c. In contrast to eq 4, eq 5 pointed out the best D^* of 8.475×10^{12} cm Hz$^{1/2}$ W^{-1} for the device with 5% MoO$_3$ dopant. In addition, from applying the approximation by further neglecting thermal noise contribution (so-called shot approximation), which was often adopted in the previous studies,[1,13,40] the best D^* is calculated to be 1.897×10^{13} cm Hz$^{1/2}$ W^{-1} (see Table S2 for comparison with previous studies). Experimentally, our result demonstrates one of the best results of D^* in the wavelength around 500−550 nm based on shot approximation. However, the comparison among these methods indicates that the approximation (eq 5) by adding two noise sources or even neglecting thermal noise may lead to an overestimated D^* and shows significant difference (1−2 orders) compared to the direct measurement (eq 4) result.
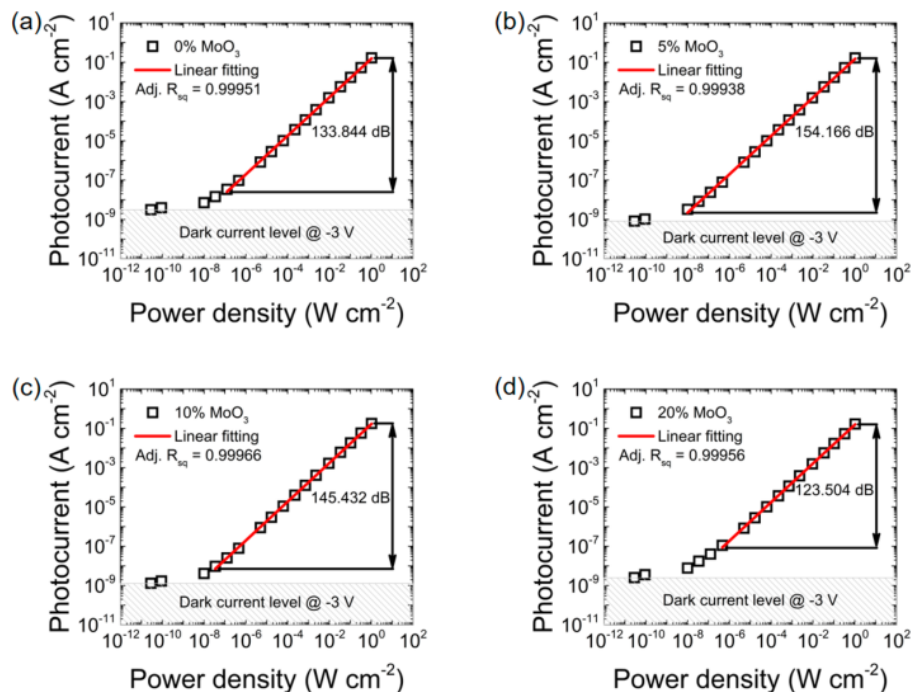
Figure 5. Measured LDR for OPD device doped with (a) 0%, (b) 5%, (c) 10%, and (d) 20% of MoO_3 under an applied bias voltage of -3 V. The OPD device is exposed to green radiance from the LED and laser with the radiant flux from 1 pW cm^{-2} to 1 W cm^{-2}. The mean square deviation (Adj. R_{sq} value) is customized from the linear fitting results.
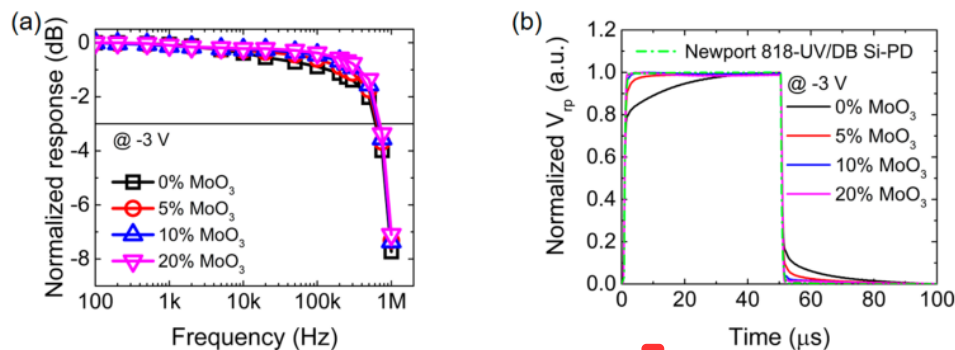

Figure 6. At an applied bias voltage of -3 V, OPD devices modulated by a green LED (525 nm) with a flux density of 1 mW cm^{-2} and recorded using an oscilloscope. Normalized dynamic characteristics refer to (a) bandwidth of frequency response from 10^{-4} to 1 MHz and (b) the pulse of TPV at a frequency of 10 kHz. The dashed line represents the pulse of Newport 818-UV/DB Si-PD.

Experimentally, the photocurrent in response to a wide range of light intensity is evaluated by linear dynamic range (LDR) measurement. Here, the indicator of linearity is defined by the change of optical power intensity with the limit levels referring to the detection of strongest to weakest photocurrent as given by[8,13,30,38,40,42−44]

$$LDR = 20 \log \left(\frac{J_{high(V)}}{J_{low(V)}} \right) \qquad (6)$$

where $J_{high(V)}$ and $J_{low(V)}$ are the upper and lower limit of photocurrent density (A cm^{-2}) by applying the same bias voltage. At a bias of -3 V, the device with 0%, 5%, 10%, and

20% of MoO_3 doped in EBL achieves an LDR of 133.844, 154.166, 145.432, and 123.504 dB, respectively (see Figure 5). Fundamentally, the nonlinear points (magnitude of LDR) under low-illumination intensities are closely related to the level of both shot (dark current) and thermal noise.[43] On the other hand, the saturation points of high-illumination intensities are limited by the trapping and carrier recombination,[42] which could be quantified by LDR measurement under zero bias voltage as presented in Figure S12. Under 0 V as presented in Table S3, except for the device with 20% MoO_3, all manifest high saturation level and wide LDR around 120 dB. This is owing to the characteristics of **DTDCPB**:C$_{70}$. Previous studies by Che et al. and Burlingame et al.

demonstrated that the strong polarity of **DTDCPB** could result in the polarization shift of the acceptor's energy level.[45,46] Such energy level shifting can form an energetic barrier near the D/A interface, confining electrons in the transporting channel and reducing electron−hole recombination loss. Therefore, combined with the lower shot and thermal noise, the device with 5% MoO_3-doped EBL exhibits the widest LDR with the value of 154.166 dB.

The characteristics of frequency response, transient photovoltage (TPV), and transient photocurrent (TPC) by an applied bias of −3 V were further investigated. The cutoff frequency, f_{-3dB}, of an OPD device indicates the limited bandwidth acquired from the signal degradation of $1/\sqrt{2}$ times when exposed by continuous illumination.[13,30] As described in Figure 6a, f_{-3dB} increases along with the doping concentration of MoO_3, with the broadest value of 692.047 kHz for the device employing EBL with 20% MoO_3 doping. To further clarify the origin of the fast response speed, f_{-3dB} is further divided into two parts, the contribution from photogenerated charge carriers and RC circuit response, which could be expressed by[8,13,43]

$$\frac{1}{f_{-3dB}^2} = (2\pi R_{tot}C)^2 + \left(\frac{2\pi t_{tr}}{3.5}\right)^2 \tag{7}$$

where R_{tot} is the total resistance (Ω, including the measuring instrument), C is the capacitance (F), and t_{tr} is the photogenerated charge carriers transport time (s). The previous studies have reported that the limited-bandwidth f_{-3dB} for the large cross-section area (4 mm^2) of the OPD device is externally governed by the equivalent circuit of RC. Thereby, the above equation can be further simplified as following[8,13,43]

$$f_{RC,-3dB} = \frac{1}{2\pi R_S C} \tag{8}$$

where R_S is the series resistance (Ω) and C is the capacitance (F). Then, the impedance spectroscopy and the corresponding Nyquist plot are conducted to fit the circuit elements, R_S, R_{CT}, and C_{DL}, where R_{CT} is the charge transfer resistance (Ω) and C_{DL} is the double-layer capacitance (F), as presented in Figure S13a.[47,48] As a consequence, the RC-based frequency response, $f_{RC,-3dB}$, is calculated with $R = R_S$ and $C = C_{DL}$, which demonstrates the enhancement trend along with the increase of the doping percentage of MoO_3. Further, these results agree well with f_{-3dB} from the oscilloscope-based measurement presented in Figure 6a, which thereby clarifies that the fastest diffusion is indeed facilitated by the interlayer of **DPSi-DBDTA**:20% MoO_3 but not instrumental artifact (see Table S4 for the summary of results).

As for time-resolved studies, both TPV and TPC present the record of time response in the form of the rising and falling times. Relating to the threshold values, the rising and falling times are determined by the time interval for the intensity to grow from 10% to 90% and drop from 90% down to 10%, respectively.[9,13] As displayed in Figure 6b, the device with EBL doped with 20% MoO_3 exhibits the fastest rise and fall times of 0.672 and 0.683 μs, respectively. The rapidity of response also agrees well with TPC (see Figure S14a and Table S5 for details). This is due to the decrease of R_S facilitated by the gap states of MoO_3.[49] For the investigation's completeness, carrier transport characteristics were evaluated via the elements of R_{CT} and C_{DL} mentioned above. Interpretations of this characteristic

led to the parameter of relaxation time constant (τ; in second), which could be estimated by the following[47,50]

$$\tau = R_{CT}C_{DL} \tag{9}$$

which is correlated with the discharge speed of accumulated carriers when the input signal suddenly turns off.[51] From the molecular level, the magnitude of R_{CT} indicates the difficulty encountered when a carrier is shifted from one molecule to another. This also experimentally connects with the pulse relaxation in the early stage of TPV and TPC (Figures S13b and S14b).

As summarized in Table S4, the device with the interlayer of **DPSi-DBDTA**:0% MoO_3 exhibits the shortest relaxation time constant τ and fastest early stage decay. This is reasonable because the existence of a gap state may increase C_{DL} due to the conductivity doping process that forms extra electron−hole pairs. Besides, the large binding energy of these electron−hole pairs leads to the difficulty (larger R_{CT}) for the carriers' hopping, rendering trap-assisted recombination.[52−54] Such results also correlate with the slightly decreased EQE in the MoO_3-doped devices. This may potentially influence response speed because C_{DL} is encoded in $f_{RC,-3dB}$. However, according to eq 8, R_S also affects $f_{RC,-3dB}$, and the lack of MoO_3 leads to a significantly higher R_S (see Table S4). Overall, the reduction of R_S outcompetes the increase of C_{DL} and leads to the fastest late-stage decay and frequency response for the 20% MoO_3-doped device. Intriguingly, for all the devices with MoO_3-doped EBL, regardless of the slight difference for final-stage decay as demonstrated in Figures S13c and S14c, t_{Fall} and t_{Rise} are in the submicrosecond region (both TPV and TPC results). Compared with the transient response with bare EBL, it enhances more than one order as MoO_3 doped in EBL, especially for t_{Rise}, which reduces from around 10 to 0.9 μs. It is possibly attributed to the enhancement of hole mobility in the MoO_3-doped device. However, on the basis of our measurement, the increment of hole mobility is quite limited (less than one order; see Table 1). Therefore, we rationalize this issue to the carrier balancing in EBL. Due to the high LUMO of **DPSi-DBDTA**, the electron diffusion length is very short in EBL, which can be verified by its low mobility ($\mu_e = 1.418 \times 10^{-12}$ cm^2 V^{-1} s^{-1}).

As well studied by Goodman et al., under the illumination of light, if one of the carriers' diffusion lengths (ω) is much longer than the other, in our case, $\omega_h \gg \omega_e$, the accumulated, slowly transported carriers may form an electric field that tilts the band structure and reduces the overall extraction efficiency.[55] However, the situation changes when the MoO_3 is introduced, where much balanced mobility is achieved (both μ_e and μ_h of $\sim 10^{-6}$ cm^2 V^{-1} s^{-1}), therefore resulting in better transportation behavior. Consequently, although the existence of MoO_3 may form deep traps, the balancing of mobility mitigates these phenomena, experimentally connecting with the fact of decreased R_S outcompeting the increase of C_{DL}. All of the above unique features are owing to the interaction between **DPSi-DBDTA** and MoO_3 that achieves this balance. Eventually, the EBL by doping percentage of MoO_3 of 20% leads to the value of t_{Fall} of 0.683 μs, which is comparable to the Si-PDs (0.640 μs) and the best of perovskite-PDs (0.3−10 μs).[37,38,44,56,57] To the best of our knowledge, our current result is one of the best cases ever reported for the vacuum-processed OPDs (Table S2). These results manifest the great potential of this new OPD device for fast time-resolved imaging, i.e., tracing photoluminescence decay, optical

communication technology, and other applications that require kHz detection speed. For the stability trial, the power density was set up at an intensity of 1 mW cm^{-2} to generate prolonged illuminance of white light (5700 K); both illumination and dark conditions are evaluated for 120 h as plotted in Figure S15a. As shown in Figure S15b, the photoconversion efficiency of the OPD device was plotted and compared with that of the Si-based photodetector (Hamamatsu S1337). Both results, including dark current and EQE, show no significant changes after 120 h, which guarantees the stability of our devices.

3. CONCLUSION

A new EBL **DPSi-DBDTA** comprising an aryldiamine and dioxasilepine was synthesized and characterized. The introduction of dioxasilepine endows the new molecule with high thermal and morphological stability and the dipolar character verified by the DFT calculation at the B3LYP/6-31G (d,p) level. **DPSi-DBDTA** exhibits a high LUMO that is mainly populated on the dioxasilepine and the biphenyl core. Analysis of the crystal structure indicates that the dipolar feature leads **DPSi-DBDTA** molecules to pack into an antiparallel packing manner with the twisted dioxasilepine structure preventing neighboring molecules from π–π interacting. The high LUMO of **DPSi-DBDTA** ensures its propensity to serve as an EBL in OPD, which was verified by OPD with the single active layer C_{60}, giving a dark current density as low as $\sim 10^{-11}$ A cm^{-2} under a bias of −1 to −2 V that outperforms the conventional aryldiamine-based EBLs. **DPSi-DBDTA** was further manifested as a good EBL in the visible-light-responsive OPD structure, composing it with the **DTDCPB**:C_{70} blend as a BHJ-type active layer. For further modification of EBLs' transportation behavior, different doping percentages of MoO_3 were doped into the EBL. Under the dark condition, the device with 5% MoO_3 dopant exhibits the best dark current suppression. Together with V_{OC} increment, we ascribed such phenomena to the formation of a dipole interlayer. Similarly, the result of R_{Sh} pointed out that the device with 5% MoO_3-doped EBL has the highest value of 0.410 GΩ, which indicates that, not only dark current, thermal leakage from the active layer can also be further prevented by dipole interlayer formation. In sync with the above measurements, the device with 5% MoO_3-doped EBL exhibits the broadest LDR of 154.166 dB under −3 V. Nonetheless, on the basis of the white noise current calculation, the device with bare EBL shows the best D^* of 7.085×10^{12} cm Hz$^{1/2}$ W^{-1}, which points out that other types of noise are unavailable for decoupling by conventional methods instead of direct measurements.

The AFM analysis was carried out to understand the interaction between **DPSi-DBDTA** and MoO_3 further. It reveals the enhancement of **DPSi-DBDTA**'s crystallinity through the interaction with MoO_3. This is further verified by carrier mobility characterizations, where the 6 order enhancement in electron mobility was observed. Such phenomena can then rationalize the fast response speed of the device, where a wide cutoff frequency response of ~ 692.047 kHz and a Si-PDs-comparable t_{Fall} of ~ 0.68 μs (for TPV) were recorded in the device with **DPSi-DBDTA**:20% MoO_3 as an EBL. Our work reveals the critical roles of mobility, recombination, noise, and relationships with EBL properties. Besides, the functions of metal oxide, its interaction with EBL, and the influence on bulk properties are explored. Finding a suitable EBL and its modification are of primary importance for a low-recombination active layer of the

OPD device. Consequently, the introduction of MoO_3 in the designated EBL for enhancing the conductivity and adjusting the mobility can potentially furnish low noise, fast response, and eventually a highly efficient OPD.

4. EXPERIMENTAL SECTION

The detailed synthetic procedure and characterization of the final compounds are provided in the Supporting Information. In this study, the structures of OPD device are fabricated as follows: (1) ITO/**NPB** (20 nm)/C_{60} (80 nm)/Bphen (3 nm)/Ag (120 nm), (2) ITO/**TAPC**:$xMoO_3$ ($x = 0\%$, 5%, 10%, and 20%; 20 nm)/C_{60} (80 nm)/Bphen (3 nm)/Ag (120 nm), (3) ITO/**TAPC**:xWO_3 ($x = 0\%$, 5%, 10%, and 20%; 20 nm)/C_{60} (80 nm)/Bphen (3 nm)/Ag (120 nm), (4) ITO/**DPSi-DBDTA**:$xMoO_3$ ($x = 0\%$, 5%, 10%, and 20%; 20 nm)/**DTDCPB**:C_{60} (1:2; 80 nm)/Bphen (3 nm)/Ag (120 nm), and (5) ITO/**DPSi-DBDTA**:$xMoO_3$ ($x = 0\%$, 5%, 10%, and 20%; 20 nm)/**DTDCPB**:C_{70} (1:2; 80 nm)/Bphen (3 nm)/Ag (120 nm).

NMR spectra were measured in $CDCl_3$ and CD_2Cl_2 using a Varian (Utility 400) spectrometer for ^{1}H NMR (400 MHz) and ^{13}C NMR (100 MHz). Optical absorption and emission measurements were conducted by a JASCO V-670 spectrophotometer and Hitachi F-4500 spectrometer, respectively. The concentration of the sample is about 4×10^{-5} M dissolved in toluene. Thermogravimetric analysis (TGA) was conducted under a nitrogen atmosphere at a heating rate of 10 °C min^{-1} on a platinum pan via a TA Instruments Q500 TGA (V20.13 Build 39). Differential scanning calorimetry (DSC) analyses were performed on a TA Instruments DSC-2920 low temperature difference scanning calorimetry at a heating rate of 10 °C min^{-1} under nitrogen atmosphere. The electrochemical properties were measured by cyclic voltammetry (CHI619B potentiostat). A glassy carbon electrode was used as a working electrode, and a platinum wire was used as a counter electrode. The oxidation potentials were conducted in dried dichloromethane (1.0 mM) with 0.1 M tetrabutylammonium hexafluorophosphate ($^nBuNPF_6$) as the supporting electrolyte, which was recorded versus Ag/AgCl as a reference electrode, and further calibrated with the ferrocene/ferrocenium (Fc/Fc$^+$) redox couple. The mass spectra were recorded by the National Taiwan University Mass Spectrometry-based Proteomics Core Facility of Bruker Daltonics Autoflex speed in MALDI-TOF mode. Crystallographic data were carried out at 200(2) K on an Oxford Gemini A CCD diffractometer using with Mo Kα radiation ($\lambda = 0.710\,73$ Å). Cell parameters and data reduction were retrieved and refined manipulating CrysAlis Pro software on all reflections. The structures were solved and refined with the SHELXL programs. The hydrogen atoms were included in calculated positions and refined using a riding mode.

In the dark condition and under AM 1.5G solar simulator irradiation (Newport, 91160A) with an intensity of 100 mW cm^{-2}, the current density–voltage (J–V) characteristics by sweep measurement mode were recorded using a unit of programmable source meter (Keithley, model 2636A). On the range frequency of 300–850 nm, the spectrum of EQE and responsivity were recorded in DC mode using QE-R systems (Enlitech, Taiwan) with Si-based photodetector (Hamamatsu S1337) that was procedurally using to calibrate monochromatic light beams. This was carried out according to the standard of IEC 60904-8:20146. The external equivalent circuit combination was identified using electrochemical impedance spectroscopy (Solartron, Materials Lab XM) with a signal of sinusoidal AC (an amplitude of 1.5 V) analyzed under a swept-frequency mode of 10^{-6} to 1 MHz. In computer-based data-acquisition systems, the LabView software was developed by Enlitech (Enli Technology Co., Ltd., Taiwan), which allows controlling of the setup and displaying of the noise current power spectral density using the source measure unit instrument (Keithley, model 2636A). For measurement of LDR, the light beams of the laser (CNI, MGL-III-532) and LED (Thorlabs, M530L3) with respective emission wavelengths of 532 and 530 nm were pointing to a motor-driven filter wheel (Thorlabs, FW12CNEB), which generates a controlled light intensity to the area of the OPD device. For the frequency response and transient

response of OPDs, a commercial LED (Thorlabs, the emission wavelength of 525 nm) that was tuned in a flux density of 1 mW cm^{-2} was connected to a function generator (Tektronix, AFG3102C), which generates the pulse to trigger out the device of OPDs. The output pulse from the OPD device was amplified by a preamplifier that operates in the low noise current with an A/V gain factor of 10^{-6}, then captured and plotted by a 2.5 GHz oscilloscope (Teledyne LeCroy, WaveRunner 625Zi), while Newport 818-UV/DB Si-PD was used as a comparison pulse. Further, an LED white light (5700 K) was tuned to the intensity of 1 mW cm^{-2} by using a spectrum meter (Optimum, SRI-2000), intended for the stability trial of the OPD device.

■ ASSOCIATED CONTENT

ⓢ Supporting Information

The Supporting Information is available free of charge at https://pubs.acs.org/doi/10.1021/acsami.2c04434.

Synthesis detail, TGA and DSC profiles of **DPSi-DBDTA**, OPDs device layer structure, $J-V$ characteristics, AFM images, themal noise current PSD−frequency, EQE profiles, responsivity, D*, LDR, Nyquist plot, initial and final pulsed relaxation, and stability trial (PDF)

■ AUTHOR INFORMATION

Corresponding Authors

Shun-Wei Liu − Organic Electronics Research Center and Department of Electronic Engineering, Ming Chi University of Technology, New Taipei City 24301, Taiwan; ⓞ orcid.org/0000-0002-3128-905X; Email: swliu@mail.mcut.edu.tw

Ken-Tsung Wong − Department of Chemistry, National Taiwan University, Taipei 10617, Taiwan; Present Address: Institute of Atomic and Molecular Science, Academia Sinica, Taipei 10617, Taiwan; ⓞ orcid.org/0000-0002-1680-6186; Email: kenwong@ntu.edu.tw

Authors

Kai-Hua Kuo − Department of Chemistry, National Taiwan University, Taipei 10617, Taiwan

Richie Estrada − Organic Electronics Research Center and Department of Electronic Engineering, Ming Chi University of Technology, New Taipei City 24301, Taiwan; Department of Electronic Engineering, National Taiwan University of Science and Technology, Taipei 10607, Taiwan

Chih-Chien Lee − Department of Electronic Engineering, National Taiwan University of Science and Technology, Taipei 10607, Taiwan

Nurul Ridho Al Amin − Organic Electronics Research Center and Department of Electronic Engineering, Ming Chi University of Technology, New Taipei City 24301, Taiwan; Department of Electronic Engineering, National Taiwan University Science and Technology, Taipei 10607, Taiwan

Ya-Ze Li − Organic Electronics Research Center and Department of Electronic Engineering, Ming Chi University of Technology, New Taipei City 24301, Taiwan; Department of Electronic Engineering, National Taiwan University of Science and Technology, Taipei 10607, Taiwan

Marvin Yonathan Hadiyanto − Organic Electronics Research Center and Department of Electronic Engineering, Ming Chi University of Technology, New Taipei City 24301, Taiwan

Complete contact information is available at:
https://pubs.acs.org/10.1021/acsami.2c04434

■ REFERENCES

(1) Simone, G.; Dyson, M. J.; Meskers, S. C. J.; Janssen, R. A. J.; Gelinck, G. H. Organic Photodetectors and Their Application in Large Area and Flexible Image Sensors: The Role of Dark Current. Adv. Funct. Mater. 2020, 30, 1904205.

(2) Ren, H.; Chen, J.-D.; Li, Y.-Q.; Tang, J.-X. Recent Progress in Organic Photodetectors and Their Applications. Adv. Sci. 2021, 8, 2002418.

(3) Gong, X.; Tong, M.; Xia, Y.; Cai, W.; Moon, J. S.; Cao, Y.; Yu, G.; Shieh, C.-L.; Nilsson, B.; Heeger, A. J. High-Detectivity Polymer Photodetectors with Spectral Response from 300 Nm to 1450 Nm. Science 2009, 325, 1665−1667.

(4) Kamada, T.; Hatsumi, R.; Watanabe, K.; Kawashima, S.; Katayama, M.; Adachi, H.; Ishitani, T.; Kusunoki, K.; Kubota, D.; Yamazaki, S. OLED Display Incorporating Organic Photodiodes for Fingerprint Imaging. J. Soc. Inf. Dispersion 2019, 27, 361−371.

(5) Fuentes-Hernandez, C.; Chou, W.-F.; Khan, T. M.; Diniz, L.; Lukens, J.; Larrain, F. A.; Rodriguez-Toro, V. A.; Kippelen, B. Large-Area Low-Noise Flexible Organic Photodiodes for Detecting Faint Visible Light. Science 2020, 370, 698−701.

(6) Chen, Y.-H.; Lin, L.-Y.; Lu, C.-W.; Lin, F.; Huang, Z.-Y.; Lin, H.-W.; Wang, P.-H.; Liu, Y.-H.; Wong, K.-T.; Wen, J.; Miller, D. J.; Darling, S. B. Vacuum-Deposited Small-Molecule Organic Solar Cells with High Power Conversion Efficiencies by Judicious Molecular Design and Device Optimization. J. Am. Chem. Soc. 2012, 134, 13616−13623.

(7) Xiong, S.; Li, L.; Qin, F.; Mao, L.; Luo, B.; Jiang, Y.; Li, Z.; Huang, J.; Zhou, Y. Universal Strategy To Reduce Noise Current for Sensitive Organic Photodetectors. ACS Appl. Mater. Interfaces 2017, 9, 9176−9183.

(8) Lee, C.-C.; Biring, S.; Ren, S.-J.; Li, Y.-Z.; Li, M.-Z.; Al Amin, N. R.; Liu, S.-W. Reduction of Dark Current Density in Organic Ultraviolet Photodetector by Utilizing an Electron Blocking Layer of TAPC Doped with MoO$_3$. Org. Electron. 2019, 65, 150−155.

(9) Zhou, X.; Yang, D.; Ma, D. Extremely Low Dark Current, High Responsivity, All-Polymer Photodetectors with Spectral Response from 300 Nm to 1000 Nm. Adv. Opt. Mater. 2015, 3, 1570−1576.

(10) Zhang, S.-S.; Zhang, X.-H.; Huang, J. Effect of Hole Transport Layers on the Performance of Organic Optoelectronic Devices Based on PBDB-T:ITIC Bulk Heterojunction. Adv. Eng. Res. 2017, 110, 71−75.

(11) Wang, M.; Li, Y.-Z.; Chen, H.-C.; Liu, C.-W.; Chen, Y.-S.; Lo, Y.-C.; Tsao, C.-S.; Huang, Y.-C.; Liu, S.-W.; Wong, K.-T.; Hu, B. Unveiling the Underlying Mechanism of Record-High Efficiency Organic near-Infrared Photodetector Harnessing a Single-Component Photoactive Layer. Mater. Horizons 2020, 7, 1171−1179.

(12) Shao, D.; Yu, M.; Sun, H.; Xin, G.; Lian, J.; Sawyer, S. High-Performance Ultraviolet Photodetector Based on Organic-Inorganic Hybrid Structure. ACS Appl. Mater. Interfaces 2014, 6, 14690−14694.

(13) Lee, C.-C.; Estrada, R.; Li, Y.-Z.; Biring, S.; Amin, N. R. A.; Li, M.-Z.; Liu, S.-W.; Wong, K.-T. Vacuum-Processed Small Molecule Organic Photodetectors with Low Dark Current Density and Strong Response to Near-Infrared Wavelength. Adv. Opt. Mater. 2020, 8, 2000519.

(14) Wang, X.; Zhou, D.; Huang, J.; Yu, J. High Performance Organic Ultraviolet Photodetector with Efficient Electroluminescence Realized by a Thermally Activated Delayed Fluorescence Emitter. *Appl. Phys. Lett.* **2015**, *107*, 043303.

(15) Lee, N.-J.; Lee, D.-H.; Kim, D.-W.; Lee, J.-H.; Cho, S. H.; Jeon, W. S.; Kwon, J. H.; Suh, M. C. Highly Efficient Soluble Materials for Blue Phosphorescent Organic Light-Emitting Diode. *Dye. Pigment.* **2012**, *95*, 221−228.

(16) Su, Z.; Wang, L.; Li, Y.; Zhao, H.; Chu, B.; Li, W. Ultraviolet-Ozone-Treated PEDOT:PSS as Anode Buffer Layer for Organic Solar Cells. *Nanoscale Res. Lett.* **2012**, *7*, 465.

(17) Bilby, D.; Frieberg, B.; Kramadhati, S.; Green, P.; Kim, J. Design Considerations for Electrode Buffer Layer Materials in Polymer Solar Cells. *ACS Appl. Mater. Interfaces* **2014**, *6*, 14964−14974.

(18) Bürckstümmer, H.; Tulyakova, E. V.; Deppisch, M.; Lenze, M. R.; Kronenberg, N. M.; Gsänger, M.; Stolte, M.; Meerholz, K.; Würthner, F. Efficient Solution-Processed Bulk Heterojunction Solar Cells by Antiparallel Supramolecular Arrangement of Dipolar Donor-Acceptor Dyes. *Angew. Chemie - Int. Ed.* **2011**, *50*, 11628−11632.

(19) Bürckstümmer, H.; Kronenberg, N. M.; Gsänger, M.; Stolte, M.; Meerholz, K.; Würthner, F. Tailored Merocyanine Dyes for Solution-Processed BHJ Solar Cells. *J. Mater. Chem.* **2010**, *20*, 240−243.

(20) Li, Y.; Chen, H.; Zhang, J. Carrier Blocking Layer Materials and Application in Organic Photodetectors. *Nanomaterials* **2021**, *11*, 1404.

(21) Anrango-Camacho, C.; Pavón-Ipiales, K.; Frontana-Uribe, B. A.; Palma-Cando, A. Recent Advances in Hole-Transporting Layers for Organic Solar Cells. *Nanomaterials* **2022**, *12*, 443.

(22) Shinmura, Y.; Yoshioka, T.; Kaji, T.; Hiramoto, M. Mapping of Band-Bending for Doped C_{60} Films. *Appl. Phys. Express* **2014**, *7*, 071601.

(23) Meyer, J.; Hamwi, S.; Kröger, M.; Kowalsky, W.; Riedl, T.; Kahn, A. Transition Metal Oxides for Organic Electronics: Energetics, Device Physics and Applications. *Adv. Mater.* **2012**, *24*, 5408−5427.

(24) Ayobi, A.; Mirnia, S. N.; Rezaee Roknabadi, M.; Bahari, A. The Effects of Molybdenum Trioxide (MoO_3) Thickness on the Improvement of Driving and Operating Voltages of Organic Light Emitting Devices. *Optoelectron. Adv. Mater. Rapid Commun.* **2019**, *13*, 519−524.

(25) Chen, L.; Chen, Q.; Wang, C.; Li, Y. Interfacial Dipole in Organic and Perovskite Solar Cells. *J. Am. Chem. Soc.* **2020**, *142*, 18281−18292.

(26) Lv, L.; Yu, J.; Hu, M.; Yin, S.; Zhuge, F.; Ma, Y.; Zhai, T. Design and Tailoring of Two-Dimensional Schottky, PN and Tunnelling Junctions for Electronics and Optoelectronics. *Nanoscale* **2021**, *13*, 6713−6751.

(27) Benatto, L.; Marchiori, C. F. N.; Talka, T.; Aramini, M.; Yamamoto, N. A. D.; Huotari, S.; Roman, L. S.; Koehler, M. Comparing C_{60} and C_{70} as Acceptor in Organic Solar Cells: Influence of the Electronic Structure and Aggregation Size on the Photovoltaic Characteristics. *Thin Solid Films* **2020**, *697*, 137827.

(28) Huang, L.; Chen, L.; Huang, P.; Wu, F.; Tan, L.; Xiao, S.; Zhong, W.; Sun, L.; Chen, Y. Triple Dipole Effect from Self-Assembled Small-Molecules for High Performance Organic Photovoltaics. *Adv. Mater.* **2016**, *28*, 4852−4860.

(29) Gao, Z.; Feng, Z.; Chen, W.; Qu, W.; Ao, W.; Yang, T.; Li, J.; Gao, F. The Application of a Non-Doped Composite Hole Transport Layer of $[MoO_3/CBP]_n$ with Multi-Periodic Structure for High Power Efficiency Organic Light-Emitting Diodes. *RSC Adv.* **2019**, *9*, 4957−4962.

(30) Strobel, N.; Seiberlich, M.; Eckstein, R.; Lemmer, U.; Hernandez-Sosa, G. Organic Photodiodes: Printing, Coating, Benchmarks, and Applications. *Flex. Print. Electron.* **2019**, *4*, 043001.

(31) Kay, A. *Operational Amplifier Noise*; Newnes: Oxford, U.K., 2012.

(32) Yang, D.; Ma, D. Development of Organic Semiconductor Photodetectors: From Mechanism to Applications. *Adv. Opt. Mater.* **2019**, *7*, 1800522.

(33) Johnson, M. *Photodetection and Measurement: Maximizing Performance in Optical Systems*; McGraw-Hill Companies, Inc.: New York, USA, 2003.

(34) Beenakker, C.; Schönenberger, C. Quantum Shot Noise. *Phys. Today* **2003**, *56*, 37−42.

(35) Lambrechts, J.; Sinha, S. Harvesting Energy from Ambient Sources: Wind Energy, Hydropower, Radiation and Mechanical Deformation. *Smart Sensors, Measurement and Instrumentation* **2016**, *18*, 101−134.

(36) Wu, Z.; Yao, W.; London, A. E.; Azoulay, J. D.; Ng, T. N. Elucidating the Detectivity Limits in Shortwave Infrared Organic Photodiodes. *Adv. Funct. Mater.* **2018**, *28*, 1800391.

(37) Fang, Y.; Huang, J. Resolving Weak Light of Sub-Picowatt per Square Centimeter by Hybrid Perovskite Photodetectors Enabled by Noise Reduction. *Adv. Mater.* **2015**, *27*, 2804−2810.

(38) Bao, C.; Chen, Z.; Fang, Y.; Wei, H.; Deng, Y.; Xiao, X.; Li, L.; Huang, J. Low-Noise and Large-Linear-Dynamic-Range Photodetectors Based on Hybrid-Perovskite Thin-Single-Crystals. *Adv. Mater.* **2017**, *29*, 1703209.

(39) Macabebe, E. Q. B.; Van Dyk, E. E. Parameter Extraction from Dark Current-Voltage Characteristics of Solar Cells. *S. Afr. J. Sci.* **2008**, *104*, 401−404.

(40) Zhong, Z.; Li, K.; Zhang, J.; Ying, L.; Xie, R.; Yu, G.; Huang, F.; Cao, Y. High-Performance All-Polymer Photodetectors via a Thick Photoactive Layer Strategy. *ACS Appl. Mater. Interfaces* **2019**, *11*, 14208−14214.

(41) Fang, Y.; Armin, A.; Meredith, P.; Huang, J. Accurate Characterization of Next-Generation Thin-Film Photodetectors. *Nat. Photonics* **2019**, *13*, 1−4.

(42) Li, W.; Xu, Y.; Meng, X.; Xiao, Z.; Li, R.; Jiang, L.; Cui, L.; Zheng, M.; Liu, C.; Ding, L.; Lin, Q. Visible to Near-Infrared Photodetection Based on Ternary Organic Heterojunctions. *Adv. Funct. Mater.* **2019**, *29*, 1808948.

(43) Armin, A.; Hambsch, M.; Kim, I. K.; Burn, P. L.; Meredith, P.; Namdas, E. B. Thick Junction Broadband Organic Photodiodes. *Laser Photonics Rev.* **2014**, *8*, 924−932.

(44) Dou, L.; Yang, Y. M.; You, J.; Hong, Z.; Chang, W.-H.; Li, G.; Yang, Y. Solution-Processed Hybrid Perovskite Photodetectors with High Detectivity. *Nat. Commun.* **2014**, *5*, 5404.

(45) Che, X.; Li, Y.; Qu, Y.; Forrest, S. R. High Fabrication Yield Organic Tandem Photovoltaics Combining Vacuum- and Solution-Processed Subcells with 15% Efficiency. *Nat. Energy* **2018**, *3*, 422−427.

(46) Burlingame, Q.; Coburn, C.; Che, X.; Panda, A.; Qu, Y.; Forrest, S. R. Centimetre-Scale Electron Diffusion in Photoactive Organic Heterostructures. *Nature* **2018**, *554*, 77−80.

(47) Sarker, S.; Ahammad, A. J. S.; Seo, H. W.; Kim, D. M. Electrochemical Impedance Spectra of Dye-Sensitized Solar Cells: Fundamentals and Spreadsheet Calculation. *Int. J. Photoenergy* **2014**, *2014*, 851705.

(48) Qu, D.; Wang, G.; Kafle, J.; Harris, J.; Crain, L.; Jin, Z.; Zheng, D. Electrochemical Impedance and Its Applications in Energy-Storage Systems. *Small Methods* **2018**, *2*, 1700342.

(49) Pockett, A.; Lee, H. K. H.; Coles, B. L.; Tsoi, W. C.; Carnie, M. J. A Combined Transient Photovoltage and Impedance Spectroscopy Approach for a Comprehensive Study of Interlayer Degradation in Non-Fullerene Acceptor Organic Solar Cells. *Nanoscale* **2019**, *11*, 10872−10883.

(50) Von Hauff, E. Impedance Spectroscopy for Emerging Photovoltaics. *J. Phys. Chem. C* **2019**, *123*, 11329−11346.

(51) Pockett, A.; Eperon, G. E.; Sakai, N.; Snaith, H. J.; Peter, L. M.; Cameron, P. J. Microseconds, Milliseconds and Seconds: Deconvoluting the Dynamic Behaviour of Planar Perovskite Solar Cells. *Phys. Chem. Chem. Phys.* **2017**, *19*, 5959−5970.

(52) Liu, M.; Chen, Z.; Yang, Y.; Yip, H. L.; Cao, Y. Reduced Open-Circuit Voltage Loss for Highly Efficient Low-Bandgap Perovskite Solar Cells: Via Suppression of Silver Diffusion. *J. Mater. Chem. A* **2019**, *7*, 17324−17333.

(53) Lian, X.; Wu, H.; Zuo, L.; Zhou, G.; Wen, X.; Zhang, Y.; Wu, G.; Xie, Z.; Zhu, H.; Chen, H. Stable Quasi-2D Perovskite Solar Cells with Efficiency over 18% Enabled by Heat−Light Co-Treatment. *Adv. Funct. Mater.* **2020**, *30*, 2004188.

(54) Li, P.; Wu, B.; Yang, Y. C.; Huang, H. S.; Yang, X. D.; Zhou, G. D.; Song, Q. L. Improved Charge Transport Ability of Polymer Solar Cells by Using NPB/MoO$_3$ as Anode Buffer Layer. *Sol. Energy* **2018**, *170*, 212−216.

(55) Goodman, A. M.; Rose, A. Double Extraction of Uniformly Generated Electron-Hole Pairs from Insulators with Noninjecting Contacts. *J. Appl. Phys.* **1971**, *42*, 2823−2830.

(56) Li, C.; Lu, J.; Zhao, Y.; Sun, L.; Wang, G.; Ma, Y.; Zhang, S.; Zhou, J.; Shen, L.; Huang, W. Highly Sensitive, Fast Response Perovskite Photodetectors Demonstrated in Weak Light Detection Circuit and Visible Light Communication System. *Small* **2019**, *15*, 1903599.

(57) Dong, R.; Fang, Y.; Chae, J.; Dai, J.; Xiao, Z.; Dong, Q.; Yuan, Y.; Centrone, A.; Zeng, X. C.; Huang, J. High-Gain and Low-Driving-Voltage Photodetectors Based on Organolead Triiodide Perovskites. *Adv. Mater.* **2015**, *27*, 1912−1918.

A New Dioxasilepine–Aryldiamine Hybrid Electron-Blocking Material for Wide Linear Dynamic Range and Fast Response Organic Photodetector

thermal stability for semi-transparent colorful organic photovoltaics exceeding 13% power conversion efficiency", Nano Energy, 2020
Publication

4	www.rsc.org Internet Source	1 %
5	Chih-Cheng Liu, Tien-Sung Lin, Sunney I. Chan, Chung-Yuan Mou. "A room temperature catalyst for toluene aliphatic C–H bond oxidation: Tripodal tridentate copper complex immobilized in mesoporous silica", Journal of Catalysis, 2015 Publication	1 %
6	Chih-Chien Lee, Sajal Biring, Shiang-Jen Ren, Ya-Ze Li, Meng-Zhen Li, Nurul Ridho Al Amin, Shun-Wei Liu. "Reduction of dark current density in organic ultraviolet photodetector by utilizing an electron blocking layer of TAPC doped with MoO3", Organic Electronics, 2018 Publication	1 %

Exclude quotes   Off
Exclude bibliography   On

Exclude matches   < 1%